THE JOURNAL OF PHYSICAL CHEMISTRY C

Article

pubs.acs.org/JPCC

# Metal-Free Magnetism and Half-Metallicity of Carbon Nitride Nanotubes: A First-Principles Study

Zhaoyong Guan,[†] Jiajun Wang,[†] Jing Huang,[†,§] Xiaojun Wu,[†] Qunxiang Li,*[,†,‡] and Jinlong Yang[†,‡]

[†]Hefei National Laboratory for Physical Sciences at the Microscale and [‡]Synergetic Innovation Center of Quantum Information and Quantum Physics, University of Science and Technology of China, Hefei, Anhui 230026, China

[§]School of Materials and Chemical Engineering, Anhui Jianzhu University, Hefei, Anhui 230601, China

**ABSTRACT:** Recently transition-metal-free magnetism and half-metallicity have drawn enormous attention due to their potential applications in spintronic devices. In this work, we examine the stability, electronic structures, and magnetic properties of single-walled $C_4N_3$ nanotubes (SWCNNTs) by performing extensive spin-polarized density functional theory calculations and molecular dynamics simulations. The theoretical results clearly reveal that all examined SWCNNTs are stable at room temperature. Armchair $(n, n)$ $(n = 4-10)$, zigzag $(n, 0)$ $(n = 7-10)$, and two helical SWCNNTs have ferromagnetic ground states. All armchair SWCNNTs are metal-free half-metals, helical SWCNNTs with small radii are bipolar magnetic semiconductors, and zigzag SWCNNTs show size dependency, in which the semiconductor-to-metal transition can be realized by increasing their radii. Moreover, the total magnetic moments of SWCNNTs can be tuned by changing the number of primary $C_4N_3$ unit cells. These findings bring us the possibility of building functional electronic/spintronic devices with SWCNNTs due to the tunable metal-free magnetism and half-metallicity.

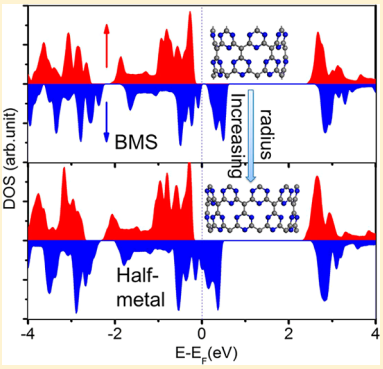


## INTRODUCTION

Metal-free magnetism and half-metallicity are at the forefront of spintronics study.[1−3] Half-metals are important spintronics materials with one metallic spin channel and another semiconducting channel, which can thus provide a completely spin-polarized current. Previous investigations have clearly revealed that many transition-metal (TM)-containing half-metals, such as manganese perovskites,[4] silicon nanowires and heterostructures,[5,6] metal−DNA complexes,[7] and Heusler compounds,[8] have robust half-metallicity. In these materials, the TMs are believed to be responsible for their half-metallicity, and the corresponding magnetism originates from TM d electrons. Note that TMs may not be compatible with many of the mature technologies, and the heavy TMs are toxic for biological systems.[9,10] Fortunately, magnetism arising from a pure 2p electron system without any TMs holds a great advantage for spintronics due to the relatively long spin relaxation time of 2p electron systems because of weak spin−orbit coupling.[11] Thus, developing metal-free ferromagnetism and non-TM half-metallic materials based on 2p elements is highly desirable.

Actually, many TM-free low-dimensional materials, including graphene nanoribbons (GNRs), boron nitride (BN) sheets, and hybrid C/BN sheets[12] and nanotubes,[13] have been predicted to be half-metallic. To realize their metal-free magnetism or half-metallicity, various strategies have been proposed.[14−30] For example, the zigzag GNRs can be tuned into half-metallic under an electric field,[14] although the required electronic field is so strong that it is hard to realize in experiments.[14,15] Kan et al.[16] and Dutta et al.[17−19] have predicted that half-metallicity in edge-modified zigzag GNRs can be realized by connecting small organic molecules or B/N dopants. Besides, line defects[20] and other defects[21] can tune the zigzag GNRs into half-metallic, and hydrogenation and fluorination of graphene or h-BN sheets have also been reported to change them to ferromagnetic and half-metallic.[22,23] However, the experimental realization of such a hydrogenation is still a big challenge, since H atoms are often formed in a random way on a host structure,[24] and they need to be produced at the plasma state at high temperature. Moreover, until now, in experiments, it has been very difficult to confirm the predicted metal-free ferromagnetism and half-metallicity.[25]

As a promising metal-free photocatalyst for water splitting,[31] recently graphitic carbon nitride (g-$C_3N_4$) with a band gap of about 2.7 eV has attracted a lot of experimental and theoretical attention.[32−38] Very recently, a new kind of graphitic carbon nitride (g-$C_4N_3$), which can be seen as C-doped graphitic $C_3N_4$, has been successfully synthesized.[39] Interestingly, this layered g-$C_4N_3$ is a ferromagnetic half-metal, which is ascribed to the substitution of one N atom by one C atom in nonmagnetic g-$C_3N_4$, resulting in one hole injected per unit cell.[40] As expected, g-$C_4N_3$ sheets can be rolled into single-walled $C_4N_3$ nanotubes (SWCNNTs), similar to $C_3N_4$ nanotubes.[41,42] This motivates us to explore the possible properties of SWCNNTs since they are unknown.

In this work, we carry out a first-principles study of the stability, electronic structures, and magnetic properties of

**Received:** January 27, 2014
**Revised:** September 6, 2014
**Published:** September 8, 2014

SWCNNTs by performing extensive density functional theory (DFT) calculations and ab initio molecular dynamics (MD) simulations. The theoretical results clearly reveal that all examined SWCNNTs are stable at room temperature. Armchair ($n$, $n$) ($n$ = 4−10), zigzag ($n$, 0) ($n$ = 7−10), and two helical SWCNNTs have ferromagnetic ground states. All armchair SWCNNTs are metal-free half-metals, helical SWCNNTs with small radii are bipolar magnetic semiconductors, and zigzag SWCNNTs display size dependency, in which the semiconductor-to-metal transition can be realized by increasing their radii. The predicted metal-free magnetism and half-metallicity of SWCNNTs lead to their great potential for functional electronic devices.

## COMPUTATIONAL DETAILS

Our calculations are performed using DFT with generalized gradient approximation (GGA) implemented with the DMol$^3$ package.[43,44] In our calculations, the exchange correlation interaction is treated by using the Perdew−Burke−Ernzerhof functional.[45] The basis set consists of the double numerical atomic orbitals augmented by polarization functions, which are comparable to Gaussian 6-31G** sets. The one-dimensional periodic boundary condition is applied along the proposed nanotube axis. The neighboring distance between the neighboring nanotubes is larger than 15.0 Å to neglect their interaction. The real-space global cutoff radius is chosen to be 4.3 Å, and 20, 40, and 104 Monkhorst−Pack[46] $k$-points are sampled for geometry optimization, total energy, and band structure calculations to sample the Brillouin zones, respectively. The calculations are all-electron ones with scalar relativistic corrections. The self-consistent field procedure is carried out with a convergence criterion of $10^{-6}$ au on the energy and electron density. Geometry optimizations are performed with convergence tolerances of $2 \times 10^{-3}$ au on the gradient, $5 \times 10^{-3}$ au on the displacement, and $1 \times 10^{-5}$ au on the energy.

A single-walled $C_4N_3$ nanotube can be constructed by rolling up a g-$C_4N_3$ sheet, as shown in the top panel of Figure 1a, along any roll-up vector. Similar to that of single-walled carbon nanotubes, the helicity of a SWCNNT is defined by a pair of integers ($m$, $n$). As examples of these examined computational models, the bottom panel of Figure 1a illustrates zigzag (10, 0), armchair (5, 5), and helical (6, 4) SWCNNTs.

To evaluate the stability of zigzag and armchair SWCNNTs, we perform ab initio MD simulations in the canonical (NVT) ensemble, in which the temperature controlled by a Nose−Hoover thermostat[47] is fixed at 300 K, the time step is 1.0 fs ($10^{-15}$ s), and the total steps are 10 000.

## RESULTS

We perform benchmark calculations for g-$C_4N_3$ sheets. The optimized results show that the g-$C_4N_3$ sheet displays an uneven structure, in which C and N atoms are not located at the same plane, and the vertical distance between two N atoms in the top and bottom outer layers is about 0.64 Å, as shown in Figure 1b. The geometric distortion of the N atom is mainly caused by the electrostatic repulsion between the neighboring N atoms charged with −0.27 e. Note that there are two different kinds of C atoms in the g-$C_4N_3$ sheet. Namely, the C atom connects to three neighboring C atoms or bonds to two neighboring N atoms and one C atom, labeled as $C_3$ and $C_N$ in Figure 1a, respectively. Due to the symmetry, there are only

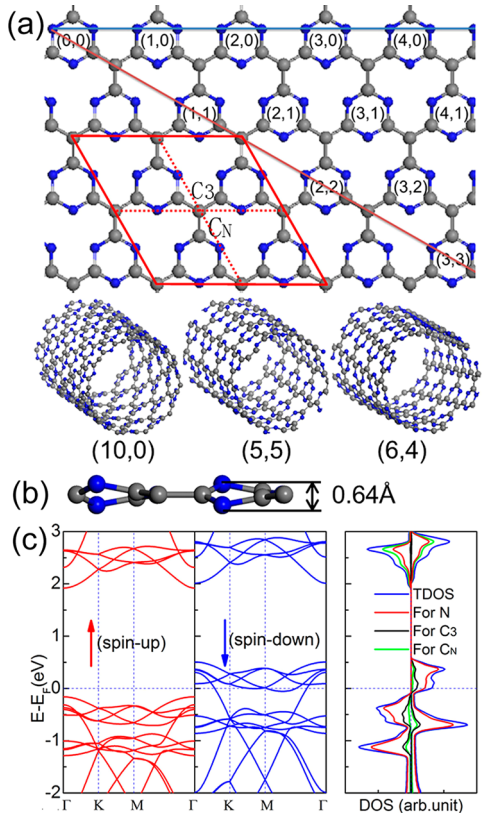


**Figure 1.** (a) Top view of the g-$C_4N_3$ sheet. The red lines label a 2 × 2 supercell, which includes four primary $C_4N_3$ unit cells. The gray and blue balls stand for C and N atoms, respectively. The zigzag (10, 0), armchair (5, 5), and helical (6, 4) SWCNNTs are plotted in the bottom panel. (b) Side view of the g-$C_4N_3$ sheet with an uneven feature. (c) Calculated spin-resolved band structures of the g-$C_4N_3$ sheet and corresponding total and partial DOSs. The Fermi level is set to zero for clarity.

two different bond lengths in the g-$C_4N_3$ sheet, and the $C_3$−$C_N$ and $C_N$−N distances are 1.46 and 1.36 Å, respectively. The energy difference ($\Delta E$) between the ferromagnetic (FM) and antiferromagnetic (AFM) states of g-$C_4N_3$ is defined as $\Delta E = E_{AFM} - E_{FM}$. Here, $E_{AFM}$ and $E_{FM}$ stand for the total energies of a 2 × 2 supercell in which four neighboring primary g-$C_4N_3$ unit cells ferromagnetically and antiferromagnetically couple with each other, respectively, similar to the previous model calculations.[40] $\Delta E$ is predicted to be 222 meV, which indicates that the ground state of the g-$C_4N_3$ sheet is ferromagnetic. Figure 1c shows the calculated spin-polarized band structures and total and partial densities of states (DOSs) of the g-$C_4N_3$ sheet. Clearly, the spin-up channel is semiconducting with a gap of 2.08 eV, while the spin-down channel is metallic. This result implies that the g-$C_4N_3$ sheet is intrinsically half-metallic. These benchmark calculated results are consistent with the previous reports[40] and also show that the methods adopted here are suitable to investigate the following examined systems.

In the optimization process, we initially construct an SWCNNT by rolling up the optimized $C_4N_3$ sheet and then fully relax all atomic positions without any constraint. In the next step we elongate and compress the lattice constant with at least five different values for each SWCNNT and fully optimize them again. According to the static self-consistently calculated total energies for these SWCNNTs with different constant lattices, it is easy to find the equilibrium lattice constant by a


dx.doi.org/10.1021/jp508617k | J. Phys. Chem. C 2014, 118, 22491−22498

polynomial curve fitting. On the basis of these equilibrium lattice constants, we fully relax all atomic positions to obtain their stable SWCNNT structures and then perform static self-consistently spin-polarized DFT calculations.

**Zigzag SWCNNTs.** We first focus on zigzag $(n, 0)$ SWCNNTs with different radii, i.e., $n$ varying from 7 to 10. As an example, the side and top views of the optimized structure of the (8, 0) zigzag SWCNNT are plotted in parts a and b, repectively, of Figure 2. In the optimized zigzag

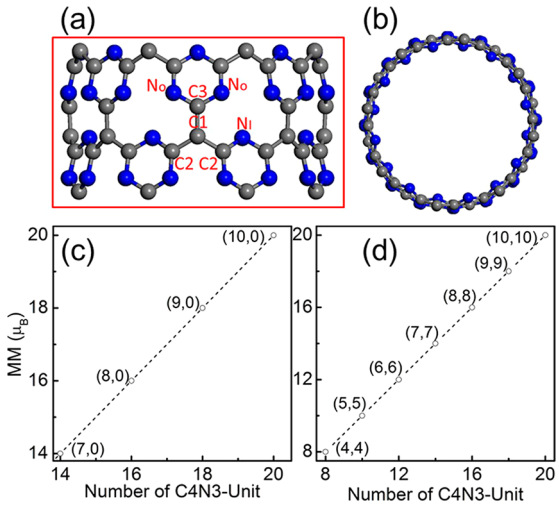


**Figure 2.** (a) Side view of the optimized zigzag (8, 0) SWCNNT. (b) Top view along the tube axis. (c) Magnetic moments of zigzag $(n, 0)$ ($n$ = 7−10) SWCNNTs. (d) Magnetic moments of armchair $(n, n)$ ($n$ = 4−10) SWCNNTs.

SWCNNTs, the N atoms move along two opposite directions and then form the inner and outside layers due to the electrostatic repulsion of the lone pair electrons localized on N atoms and the curved strain effect, while the three-coordinated C atoms located in the middle region can be divided into three types: C1, as labeled in Figure 2a, bonds to three neighboring C atoms, C2 connects to C1 and two N atoms of the inner layer ($N_I$), and C3 touches C1 and two N atoms of the outer layer ($N_O$). Here, the radii of the inner and outer layers are labeled with $r_I$ and $r_O$, respectively. We find that the radius difference ($\Delta r$) between the inner and outer layers is obvious for the zigzag SWCNNTs with a small radius, i.e., $n \leq 10$. For example, $r_I$ and $r_O$ of the (7, 0) zigzag SWCNNT are predicted to be about 4.97 and 5.71 Å, respectively. Both $C_3-C_N$ and $C_N-N$ distances in the zigzag SWCNNT become nonequivalent due to the curved effect. The $C2-N_I$, $C3-N_O$, C1−C2, and C1−C3 distances in the (8, 0) SWCNNT are 1.35, 1.36, 1.49, and 1.48 Å, respectively. Compared with the $C_3-C_N$ and $C_N-N$ distances in the g-$C_4N_3$ sheet, these values just slightly change. Note that the values of $c$ in these examined zigzag SWCNNTs are predicted to be about 8.38 Å and are insensitive to their radii.

To determine the ground states of these zigzag SWCNNTs, we compute the $\Delta E$ by performing spin-polarized calculations. We find that their ground states are all FM since the minimum of $\Delta E$ is larger than 120 meV. The predicted magnetic moments (MMs) of the zigzag $(n, 0)$ SWCNNTs with $n$ = 7−10 are plotted in Figure 2c. Clearly, the total MMs ($\mu_B$, Bohr magneton) of the zigzag SWCNNT can be linearly enhanced by increasing its radius. Similar to the g-$C_4N_3$ sheet, each primary $C_4N_3$ cell contributes 1 $\mu_B$, in which the spin density mainly localizes on N atoms and the atomic MM of each N atom is 0.33 $\mu_B$. In the zigzag (7, 0) SWCNNT, there are 14 primary $C_4N_3$ unit cells. Therefore, the total MM of the zigzag (7, 0) SWCNNT is 14 $\mu_B$. This observation is the same for the examined zigzag SWCNNTs, which implies that the MM can be tuned by changing the number of primary $C_4N_3$ unit cells.

Figure 3 shows the calculated band gaps ($E_g$) of zigzag SWCNNTs with different radii. It is clear that the band gaps of

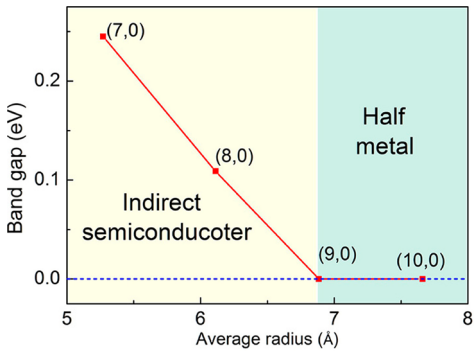


**Figure 3.** Band gaps of zigzag $(n, 0)$ SWCNNTs with $n$ = 7−10. The yellow area is for the indirect semiconducting zigzag SWCNNTs, while the green area is for the half-metals.

zigzag SWCNNTs strongly depend on their size. These zigzag SWCNNTs with relatively small radii (i.e., $n \leq 8$) are semiconductors. Their band gaps decrease with an increase of their radii. For example, the band gaps of zigzag SWCNNTs with $n$ = 7 and 8 are 0.25 and 0.11 eV, respectively. This observation is contrary to that of the $C_3N_4$ nanotubes,[41] whose band gaps increase with an increase of their radii.[42] Interestingly, we observe that the electronic structures of zigzag SWCNNTs also display size dependency. When $n \geq 9$, i.e., the (10, 0) zigzag SWCNNT, the band gap is zero. This indicates that the zigzag SWCNNT with a relatively large radius (i.e., $n \geq 9$) becomes metallic with a zero band gap. These observations provide us the opportunity to realize the semiconductor-to-metal transition in zigzag SWCNNTs by increasing their radii.

To explore the electronic structures of zigzag SWCNNTs, we take (8, 0) and (9, 0) SWCNNTs as examples. Figure 4a shows the spin-polarized band structures of the (8, 0) SWCNNT at the FM ground state. It is clear that it is a semiconductor with an indirect gap. The energy gaps of the spin-up and spin-down states are 2.67 and 0.11 eV, respectively. The band structures of the (8, 0) SWCNNT at the AFM state are plotted in Figure 4b. Clearly, it is also a semiconductor with an indirect gap of 0.08 eV, the band dispersions of the spin-up and spin-down electrons are the same, and the total MM is zero. With increasing radius, Figure 4c shows the half-metallic band structures of the (9, 0) SWCNNT. The spin-up channel has a band gap of 2.62 eV, while the spin-down channel is metallic.

To understand the electronic properties of zigzag SWCNNTs with different radii in detail, we calculate their spin-resolved DOSs. The calculated results for zigzag (7, 0) and (9, 0) SWCNNTs are plotted in parts a and b, respectively, of Figure 5. It is clear that these results verify the above observations, as shown in Figure 4. The partial DOSs (PDOSs) of C and N atoms are strongly hybridized, which leads to the covalent C−N bonds in the zigzag SWCNNT. As for the zigzag


dx.doi.org/10.1021/jp508617k | J. Phys. Chem. C 2014, 118, 22491−22498

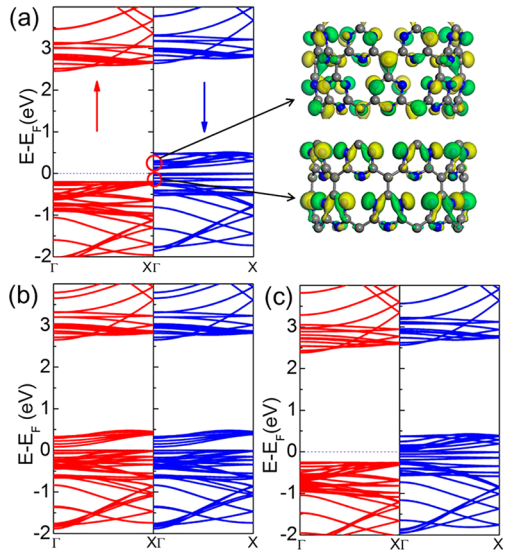


**Figure 4.** (a) Spin-resolved band structures of the zigzag (8, 0) SWCNNT at the ground FM state (left) and spatial distribution of the CBM and VBM of spin-down electrons at the Γ point (right). The isovalue is 0.02 au. (b) Band structures of the (8, 0) SWCNNT at the AFM state. (c) Band structures of the zigzag (9, 0) SWCNNT.

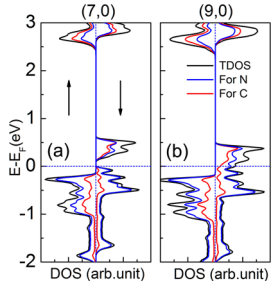


**Figure 5.** Total and partial DOSs of zigzag SWCNNTs: (a) (7, 0) and (b) (9, 0) SWCNNTs. The black, blue, and red lines stand for the total DOS and partial DOSs of N and C atoms, respectively.

SWCNNTs with a relatively small radius ($n \leq 8$), they are semiconductors, and the energy gap of their spin-down electrons is significantly less than that of the spin-up electrons. With continuously increasing radii, the broad DOS peak of the spin-down electrons gradually moves toward the Fermi level. When $n \leq 9$, the energy gap of the spin-up electrons still exists (about 2.62 eV), while the bottom conducting sub-bands of the spin-down electrons fuse with the topmost valence sub-bands, which leads to the half-metallicity of the (9, 0) SWCNNT. The calculated PDOSs for the (9, 0) SWCNNT are shown in Figure 5b. It is clear that the valence bands are mainly contributed by the N atoms, while the conduction bands are cocontributed by C and N atoms. This is in line with the g-$C_4N_3$ sheet.[40] In other words, the bigger the radius, the smaller the curve effect, and then the electronic properties of the zigzag SWCNNT become more similar to the properties of the g-$C_4N_3$ sheet.

The right panel of Figure 4a presents the spatial profile of the conduction band minimum (CBM) and the valence band maximum (VBM) of spin-down electrons at the Γ point. Through further analysis, we find that the VBM of the (8, 0) SWCNNT is mainly contributed by the $p_x$ and $p_y$ orbitals of the N atoms, while the CBM mainly comes from the N $p_z$ and C $p_z$ orbitals, exhibiting $\pi$-like bonding character. According to the Hirshfeld analysis of the population, the N atoms in the inner layer (labeled with $N_I$ in Figure 2a) get about 0.13 e from the neighboring C atoms, the N atoms in the outer layer (labeled with $N_O$) obtain 0.12 e, and the C atoms labeled with C1 and C2, lose about 0.04 and 0.12 e, respectively. It is easy to understand the net different charge transfer of C and N atoms since their local chemical environments are different.

**Armchair SWCNNTs.** In general, there are two typical edges in nanotubes, namely, zigzag and armchair edges. Now we turn to examine armchair SWCNNTs from (4, 4) to (10, 10). The top and side views of armchair (4, 4) SWCNNTs are plotted in Figure 6a. According to the optimized structures, we

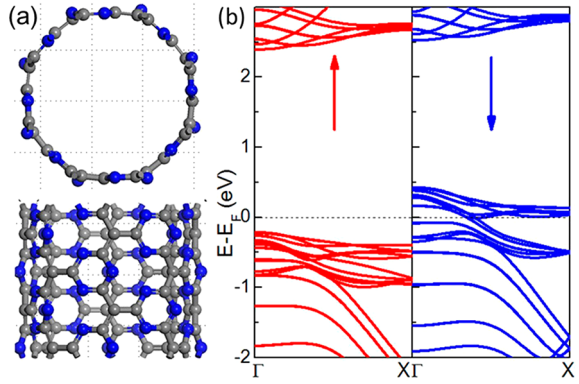


**Figure 6.** (a) Top and side views of the armchair (4, 4) SWCNNT. (c) Spin-resolved band structure of the armchair (4, 4) SWCNNT.

find that the lattice constants along the tube axis are all about 9.70 Å, and the C−C and C−N bond lengths in these armchair nanotubes vary from 1.45 to 1.34 Å and from 1.46 and 1.35 Å, respectively. These values are close to that of the g-$C_4N_3$ sheet.[40] Note that these armchair SWCNNTs with different radii show different polygons along the direction of the nanotube axis. This feature is especially obvious for the armchair SWCNNTs with a small radius since the smaller radius nanotube suffers from stronger strain, resulting in the obvious geometric deformation. For example, the (4, 4) armchair SWCNNT displays an octagon-like shape, as shown in Figure 6a. When the radius increases, the armchair SWCNNTs (i.e., $n \geq 6$) are well-ordered with a circle feature.

The minimum of $\Delta E$ per primary g-$C_4N_3$ unit cell in armchair SWCNNTs is predicted to be about 31 meV. This shows that the ground states of all armchair ($n$, $n$) SWCNNTs for $n$ = 4−10 are ferromagnetic. According to the calculated band structures, we find that all examined SWCNNTs are half-metallic. Figure 6b plots the band structure of the (4, 4) SWCNNT. Clearly, the spin-down channel is conducting, but the spin-up channel is semiconducting with a gap of 2.62 eV, similar to the half-metallicity of the g-$C_4N_3$ sheet.[40]

**Helical SWCNNTs.** To clearly explore the effect of chirality on electronic and magnetic properties, two helical SWCNNTs are also examined. Due to the helicity, there are too many atoms in the supercell to model the system. For example, the computational model for the helical (6, 4) SWCNNT contains 532 atoms (304 C atoms and 228 N atoms), and the corresponding lattice constant along the tube axis is about 58.68 Å. Because the computing cost for these helical SWCNNTs with relatively large radii is not bearable for our current computational resources, we take the (3, 2) SWCNNT as an example to explore the electronic properties. Its ground state is confirmed to be FM. The total MM is predicted to 32


dx.doi.org/10.1021/jp508617k | J. Phys. Chem. C 2014, 118, 22491−22498

$\mu_B$, which is equal to the number of primary $C_4N_3$ cells in the computational model. Parts a and b of Figure 7 show the band

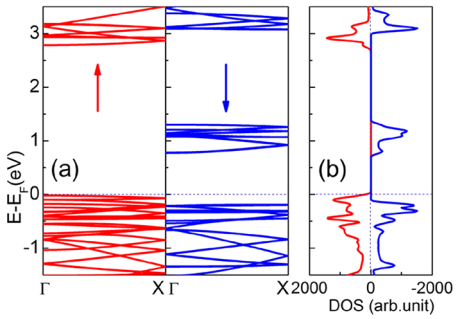


**Figure 7.** (a) Spin-resolved band structure of the helical (3, 2) SWCNNT. (b) Corresponding total DOS.

structures and DOSs of the helical (3, 2) SWCNNT, respectively. It is clear that the helical (3, 2) SWCNNT is a semiconductor with a direct band gap. The band gap of the spin-up electrons is about 2.80 eV, which is significantly larger than that of the spin-down electrons (0.97 eV). We find that the gap of the spin-down electrons can be gradually reduced by increasing the helical SWCNNT radius; i.e., it is about 0.63 eV for the helical (6, 4) SWCNNT.

It should be pointed out that the unique feature of the calculated spin-polarized PDOS, as shown in Figure 7b, indicates that the helical SWCNNTs with a relatively small radius are bipolar magnetic semiconductors (BMSs).[48] By applying a gate voltage or carrier doping, it is easy to create the completely spin-polarized currents with reversible spin polarization in BMSs. Thus, we also expect that the helical SWCNNTs have the potential for various applications, e.g., as a field effect spin rectifier.

**Stability of SWCNNTs.** It is useful to check the stability of these proposed zigzag and armchair SWCNNTs relative to the g-$C_4N_3$ sheet, which can provide a possible explanation for the rolling up of the tubes. Here, the stability of SWCNNTs is defined by the strain energies ($E_s$), defined as $E_s = E_{tube} - E_{sheet}$, where $E_{tube}$ and $E_{sheet}$ stand for the total energy of the SWCNNTs and the corresponding unrolled g-$C_4N_3$ sheet, respectively. The positive value of $E_s$ denotes that this SWCNNT is less stable than the g-$C_4N_3$ sheet. The calculated $E_s$ values of these zigzag ($n$, 0) ($n$ = 7−10) and armchair ($n$, $n$) ($n$ = 4−10) SWCNNTs are plotted in parts a and b, respectively, of Figure 8. As for the ($n$, 0) SWCNNTs, it is expected that the SWCNNTs with a relatively small radius (i.e., $n \leq 9$) have positive strain energies due to the curvature effect. With increasing radius, the stability of these zigzag SWCNNTs gradually approaches the stability of the g-$C_4N_3$ sheet. Note that $E_s$ is predicted to be −0.07 eV for the zigzag (10, 0) SWCNNT. This negative strain energy suggests that the zigzag (10, 0) SWCNNT is more stable than the g-$C_4N_3$ sheet, indicating that it is the zigzag (10, 0) SWCNNT with the smallest radius, which may be automatically produced in experiments.

As seen in Figure 8b, the stability of the examined armchair SWCNNTs can be enhanced by increasing their radii, similar to the zigzag SWCNNTs. The armchair (7, 7) SWCNNT is the first one whose stability is better than that of the g-$C_4N_3$ sheet. The calculated $E_s$ of the (7, 7) tube (its average radius is about 9.22 Å) is −0.06 eV. Clearly, all armchair SWCNNTs with $n \geq$

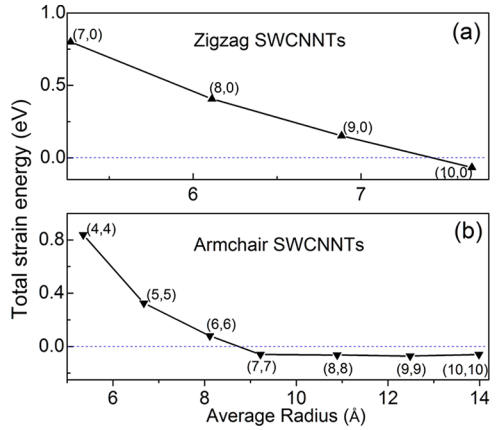


**Figure 8.** Calculated total strain energies for SWCNNTs: (a) zigzag ($n$, 0) ($n$ = 7−10) SWCNNTs, (b) armchair ($n$, $n$) ($n$ = 4−10) SWCNNTs.

7 are more stable than the g-$C_4N_3$ sheet. This fact suggests that it is possible to successfully synthesize armchair SWCNNTs with a relatively large radius, i.e., 1.0 nm, in experiments.

To examine whether these SWCNNTs are stable and whether the magnetic state survives at room temperature, we perform ab initio MD simulations for SWCNNTs. As an example, the fluctuations in the total energies and snapshots of the (5, 5) SWCNNT structure are given in parts a and b, respectively, of Figure 9. It is clear that this SWCNNT is quite

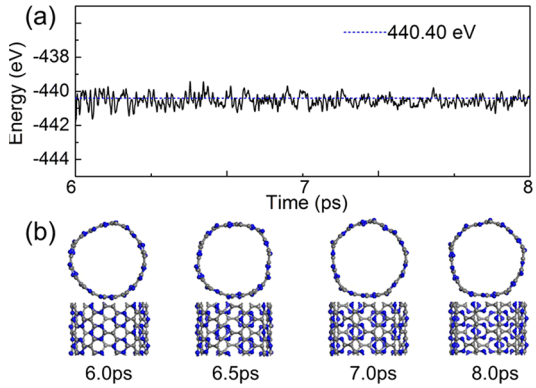


**Figure 9.** (a) Fluctuations of the total energy as a function of the MD simulation time for the (5, 5) SWCNNT. (b−e) Top and side views of snapshots at 6.0, 6.5, 7.0, and 8.0 ps of ab initio MD simulation at 300 K, respectively.

stable at room temperature. The essential tube structure is intact, although a small distortion is found. This can be understood by the fact that the binding energies of the C−N and C−C bonds are much larger than the thermal energy corresponding to the room temperature. This observation is in contrast to those for $C_3N_4$ nanotubes.[49−51] Due to the presence of relatively large holes in the g-$C_3N_4$ tubes,[50,52] their structures obviously distort. Moreover, we find that the magnetic properties are robust against structural deformation. The magnetism of the (5, 5) SWCNNT remains with an average MM of 10 $\mu_B$.

## DISCUSSION AND CONCLUSION

In general, electronic spin in elements has two $z$-components (+1/2 and −1/2), and both are equally probable. Half-metallic


dx.doi.org/10.1021/jp508617k | J. Phys. Chem. C 2014, 118, 22491−22498

ferromagnets, defined as fully spin-polarized compounds, are rare because of their unique electronic structures. In a half-metallic ferromagnet, there is a band gap at the Fermi level for the electrons of one spin direction, whereas there are sub-bands responsible for the metallic character for the electrons of the opposite spin direction, similar to the calculated results plotted in Figures 1c and 4d. All examined SWCNNTs do not have inversion symmetry, which breaks not only their time-reversal symmetry but also their conjugation symmetry. The ferromagnetism appearing in these systems may be understood by the fact that the pair of electrons (occupying a C−N bonding orbital) is broken up after injection of a hole into g-$C_4N_3$ around each substitutional N site. The observed spin-polarized electronic structures originate from the different numbers of majority and minority electrons. For the spin-up channel, the hybridization of 2p orbitals on C and N atoms leads to the separation of the $\pi$-like bonding and antibonding states by a band gap. For the spin-down electrons, the sub-bands of $2p_x$ and $2p_y$ orbitals connect with lower $2p_z$ states and are responsible for the metallic character.

It is well-known that the general gradient approximation (PBE functional adopted in this work) can be used to obtain reliable energy results. However, the size of the band gap will be underestimated. A hybrid functional, i.e. Heyd−Scuseria−Ernzerhof (HSE06),[53] is commonly expected to perform well in predicting the accurate band gap and magnetic moment. A band gap difference between PBE and hybrid functional methods can be about 1 eV in carbon-based materials. Therefore, we perform test HSE06 functional calculations by using the plane-wave basis Vienna ab initio simulation package (VASP)[54,55] to re-examine the electronic structures of the (7, 0) SWCNNT. Herein, the full potential projected plane wave framework is used with an energy cutoff of 400 eV, and the hybrid HSE06 exchange correlation functional is employed. All atoms are fully relaxed until the force on each individual atom is less than 0.02 eV/Å. The calculated spin-resolved band structures are plotted in Figure 10. Compared to the results

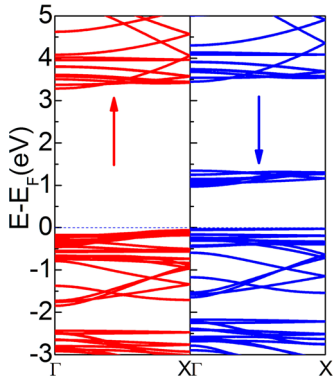


**Figure 10.** Spin-resolved band structure of the zigzag (7, 0) SWCNNT at the HSE06 hybrid functional level.

shown in Figure 5, we find that the HSE06 hybrid functional predicts similar dispersion curves of valence and conduction bands, while the position of the conduction bands is obviously up-shifted. Fortunately, the ground state remains FM, and the predicted metal-free ferromagnetism survives the choice of functional.

In conclusion, we perform extensive DFT calculations and ab initio MD simulations to explore the stability, electronic structures, and magnetic properties of zigzag, armchair, and helical SWCNNTs with small radii. Theoretical results reveal that all examined SWCNNTs are stable with ferromagnetic ground states. All armchair $C_4N_3$ nanotubes are half-metallic, the helical SWCNNTs are BMSs, and the ferromagnetic zigzag nanotubes can be tuned from semiconductor to half-metal by increasing their radii. Moreover, we find that each primary $C_4N_3$ unit contributes 1.0 $\mu_B$ to the total magnetic moments of the SWCNNTs. As a metal-free material, the SWCNNT potentially offers large spin relaxation times due to small spin−orbit coupling.[11] Our findings imply that SWCNNTs are promising candidates for future spintronics devices because of the predicted robust and tunable metal-free magnetism and half-metallicity.

## AUTHOR INFORMATION

### Corresponding Author

*E-mail: liqun@ustc.edu.cn. Phone: +86-551-63607125. Fax: +86-551-63603748.

### Notes

The authors declare no competing financial interest.

## ACKNOWLEDGMENTS

We thank Bin Li and Shuanglin Hu for useful discussions. This work was partially supported by the National Key Basic Research Program (Grants 2011CB921400 and 2014CB921101), by the Strategic Priority Research Program (B) of the Chinese Academy of Sciences (CAS; Grant XDB01020000), by the National Natural Science Foundation of China (Grants 21273208, 11034006, and 21121003), by the Anhui Provincial Natural Science Foundation (Grant 1408085QB26), by the Fundamental Research Funds for the Central Universities, by the China Postdoctoral Science Foundation (Grant 2012M511409), and by the Supercomputing Center of the Chinese Academy of Sciences (SCCAS) and Shanghai and University of Science and Technology (USTC) Supercomputer Centers.

## REFERENCES

(1) Wolf, S. A.; Awschalom, D. D.; Buhrman, R. A.; Daughton, J. M.; von Molnar, S.; Roukes, M. L.; Chtchelkanova, A. Y.; Treger, D. M. Spintronics: A Spin-Based Electronics Vision for the Future. *Science* **2001**, *294*, 1488−1495.

(2) Awschalom, D. D.; Flatte, M. E. Challenges for Semiconductor Spintronics. *Nat. Phys.* **2007**, *3*, 153−179.

(3) Felser, C.; Fecher, G. H.; Balke, B. Spintronics: A Challenge for Materials Science and Solid State Chemistry. *Angew. Chem., Int. Ed.* **2007**, *46*, 689−699.

(4) Park, J. H.; Vescovo, E.; Kim, H. J.; Kwon, C.; Ramesh, R.; Venkatesan, T. Direct Evidence for a Half-Metallic Ferromagnet. *Nature* **1998**, *392*, 794−796.

(5) Wu, H.; Kratzer, P.; Scheffler, M.; Medvedeva, J. E.; Freeman, A. J.; Cui, X. Y. Half-Metallicity and Efficient Spin Injection in AlN/GaN:Cr(0001) Heterostructure. *Phys. Rev. Lett.* **2005**, *94*, 146602.

(6) Mallajosyula, S. S.; Pati, S. K. Density-Functional Theory Study of Half-Metallic Heterostructures: Interstitial Mn in Si. *Phys. Rev. Lett.* **2007**, *98*, 117202.

(7) Mallajosyula, S. S.; Pati, S. K. Vanadium−Benzimidazole-Modified sDNA: A One-Dimensional Half-Metallic Ferromagnet. *J. Phys. Chem. B* **2007**, *111*, 13877−13880.

(8) Degroot, R. A.; Mueller, F. M.; Vanengen, P. G.; Buschow, K. H. J. New Class of Materials Half-Metallic Ferromagnets. *Phys. Rev. Lett.* **1983**, *50*, 2024−2027.

(9) Ercal, N.; Gurer-Orhan, H.; Aykin-Burns, N. Toxic Metals and Oxidative Stress Part I: Mechanisms Involved in Metal-Induced Oxidative Damage. *Curr. Top. Med. Chem.* **2001**, *1*, 529−539.
(10) Kasprzak, K. S. Oxidative DNA and Protein Damage in Metal-Induced Toxicity and Carcinogenesis. *Free Radical Biol. Med.* **2002**, *32*, 958−967.
(11) Sanvito, S. Molecular Spintronics. *Chem. Soc. Rev.* **2011**, *40*, 3336−3355.
(12) Kan, E. J.; Wu, X. J.; Li, Z. Y.; Zeng, X. C.; Yang, J. L.; Hou, J. G. Half-Metallicity in Hybrid BCN Nanoribbons. *J. Chem. Phys.* **2008**, *129*, 084712−5.
(13) Du, A.; Chen, Y.; Zhu, Z.; Lu, G.; Smith, S. C. C-BN Single-Walled Nanotubes from Hybrid Connection of BN/C Nanoribbons: Prediction by *ab Initio* Density Functional Calculations. *J. Am. Chem. Soc.* **2009**, *131*, 1682−1683.
(14) Son, Y. W.; Cohen, M. L.; Louie, S. G. Half-Metallic Graphene Nanoribbons. *Nature* **2006**, *444*, 347−349.
(15) Rudberg, E.; Salek, P.; Luo, Y. Nonlocal Exchange Interaction Removes Half-Metallicity in Graphene Nanoribbons. *Nano Lett.* **2007**, *7*, 2211−2213.
(16) Kan, E.; Li, Z.; Yang, J.; Hou, J. G. Half-Metallicity in Edge-Modified Zigzag Graphene Nanoribbons. *J. Am. Chem. Soc.* **2008**, *130*, 4224−4225.
(17) Dutta, S.; Manna, A. K.; Pati, S. K. Intrinsic Half-Metallicity in Modified Graphene Nanoribbons. *Phys. Rev. Lett.* **2009**, *102*, 096601.
(18) Dutta, S.; Pati, S. K. Half-Metallicity in Undoped and Boron Doped Graphene Nanoribbons in the Presence of Semilocal Exchange-Correlation Interactions. *J. Phys. Chem. B* **2008**, *112*, 1333−1335.
(19) Li, Y.; Zhou, Z.; Shen, P.; Chen, Z. Spin Gapless Semiconductor−Metal−Half-Metal Properties in Nitrogen-Doped Zigzag Graphene Nanoribbons. *ACS Nano* **2009**, *3*, 1952−1958.
(20) Oeiras, R. Y.; da Silva, E. Z. Defect-Mediated Half-Metal Behavior in Zigzag Graphene Nanoribbons. *Phys. Rev. B* **2009**, *80*, 073405.
(21) Lin, X.; Ni, J. Half-Metallicity in Graphene Nanoribbons with Topological Line Defects. *Phys. Rev. B* **2011**, *84*, 075461.
(22) Zhou, J.; Wang, Q.; Sun, Q.; Chen, X. S.; Kawazoe, Y.; Jena, P. Ferromagnetism in Semi-Hydrogenated Graphene Sheet. *Nano Lett.* **2009**, *6*, 3867−3870.
(23) Chen, W.; Li, Y.; Yu, G.; Li, C. Z.; Zhang, S. B.; Zhou, Z.; Chen, Z. Hydrogenation: A Simple Approach To Realize Semiconductor−Half-Metal−Metal Transition in Boron Nitride Nanoribbons. *J. Am. Chem. Soc.* **2010**, *132*, 1699−1705.
(24) Haberer, D.; Giusca, C. E.; Wang, Y.; Sachdev, H.; Fedorov, A. V.; Farjam, M.; Jafari, S. A.; Vyalikh, D. Evidence for a New Two-dimensional $C_4H$-Type Polymer Based on Hydrogenated Graphene. *Adv. Mater.* **2011**, *23*, 4497−4503.
(25) Du, A.; Smith, S. C. Electronic Functionality in Graphene-Based Nanoarchitectures: Discovery and Design via First-Principles Modeling. *J. Phys. Chem. Lett.* **2011**, *2*, 73−80.
(26) Lee, Y. L.; Kim, S.; Park, C.; Ihm, J.; Son, Y. W. Controlling Half-Metallicity of Graphene Nanoribbons by Using a Ferroelectric Polymer. *ACS Nano* **2010**, *4*, 1345−1350.
(27) Huang, B.; Si, C.; Lee, H.; Zhao, L.; Wu, J.; Gu, B. L.; Duan, W. Intrinsic Half-Metallic BN-C Nanotubes. *Appl. Phys. Lett.* **2010**, *97*, 043115−3.
(28) Du, A.; Chen, Y.; Zhu, Z.; Amal, R.; Lu, G. Q.; Smith, S. C. Dots versus Antidots: Computational Exploration of Structure, Magnetism, and Half-Metallicity in Boron−Nitride Nanostructures. *J. Am. Chem. Soc.* **2009**, *131*, 17354−17359.
(29) Zheng, F.; Zhou, G.; Liu, Z.; Wu, J.; Duan, W.; Gu, B.-L.; Zhang, S. B. Half Metallicity along the Edge of Zigzag Boron Nitride Nanoribbons. *Phys. Rev. B* **2008**, *78*, 205415.
(30) Liu, Y. L.; Wu, X. J.; Zhao, Y.; Zeng, X. C.; Yang, J. L. Half-Metallicity in Hybrid Graphene/Boron Nitride Nanoribbons with Dihydrogenated Edges. *J. Phys. Chem. C* **2011**, *115*, 9442−9450.
(31) Wang, X.; Maeda, K.; Thomas, A.; Takanabe, K.; Xin, G.; Carlsson, J. M.; Domen, K.; Antonietti, M. A Metal-Free Polymeric Photocatalyst for Hydrogen Production from Water under Visible Light. *Nat. Mater.* **2009**, *8*, 76−79.
(32) Li, X. H.; Chen, J. S.; Wang, X.; Sun, J.; Antonietti, M. Metal-Free Activation of Dioxygen by Graphene/g-$C_3N_4$ Nanocomposites: Functional Dyads for Selective Oxidation of Saturated Hydrocarbons. *J. Am. Chem. Soc.* **2011**, *133*, 8074−8077.
(33) Du, A.; Sanvito, S.; Li, Z.; Wang, D.; Jiao, Y.; Liao, T.; Sun, Q.; Ng, Y. H.; Zhu, Z.; Amal, R.; Smith, S. C. Hybrid Graphene and Graphitic Carbon Nitride Nanocomposite: Gap Opening, Electron-Hole Puddle, Interfacial Charge Transfer, and Enhanced Visible Light Response. *J. Am. Chem. Soc.* **2012**, *134*, 4393−4397.
(34) Ge, L.; Han, C.; Xiao, X.; Guo, L. Synthesis and Characterization of Composite Visible Light Active Photocatalysts $MoS_2$-g-$C_3N_4$ with Enhanced Hydrogen Evolution Activity. *Int. J. Hydrogen Energy* **2013**, *38*, 6960−6969.
(35) Hou, Y.; Laursen, A. B.; Zhang, J.; Zhang, G.; Zhu, Y.; Wang, X.; Dahl, S.; Chorkendorff, I. Layered Nanojunctions for Hydrogen-Evolution Catalysis. *Angew. Chem., Int. Ed.* **2013**, *52*, 3621−3625.
(36) Liu, G.; Niu, P.; Sun, C.; Smith, S. C.; Chen, Z.; Lu, G. Q.; Cheng, H. M. Unique Electronic Structure Induced High Photoreactivity of Sulfur-Doped Graphitic $C_3N_4$. *J. Am. Chem. Soc.* **2010**, *132*, 11642−11648.
(37) Zhang, Z.; Long, J.; Yang, L.; Chen, W.; Dai, W.; Fu, X.; Wang, X. Organic Semiconductor for Artificial Photosynthesis: Water Splitting into Hydrogen by a Bioinspired $C_3N_3S_3$ Polymer under Visible Light Irradiation. *Chem. Sci.* **2011**, *2*, 1826−1830.
(38) Dong, G.; Zhao, K.; Zhang, L. Carbon Self-Doping Induced High Electronic Conductivity and Photoreactivity of g-$C_3N_4$. *Chem. Commun.* **2012**, *48*, 6178−6180.
(39) Lee, J. S.; Wang, X.; Luo, H.; Dai, S. Fluidic Carbon Precursors for Formation of Functional Carbon under Ambient Pressure Based on Ionic Liquids. *Adv. Mater.* **2010**, *22*, 1004−1007.
(40) Du, A.; Sanvito, S.; Smith, S. C. First-Principles Prediction of Metal-Free Magnetism and Intrinsic Half-Metallicity in Graphitic Carbon Nitride. *Phys. Rev. Lett.* **2012**, *108*, 197207.
(41) Tahir, M.; Cao, C.; Butt, F. K.; Idrees, F.; Mahmood, N.; Ali, Z.; Aslam, I.; Tanveer, M.; Rizwan, M.; Mahmood, T. Tubular Graphitic-$C_3N_4$: A Prospective Material for Energy Storage and Green Photocatalysis. *J. Mater. Chem.* **2013**, *1*, 13949−13955.
(42) Gracia, J.; Kroll, P. First Principles Study of $C_3N_4$ Carbon Nitride Nanotubes. *J. Phys. Chem. A* **2007**, *111*, 5678−5684.
(43) Delley, B. An All-Electron Numerical Method for Solving the Local Density Functional for Polyatomic Molecules. *J. Chem. Phys.* **1990**, *92*, 508−517.
(44) Delley, B. From Molecules to Solids with the $DMol^3$ Approach. *J. Chem. Phys.* **2000**, *113*, 7756−7764.
(45) Perdew, J. P.; Burke, K.; Ernzerhof, M. Generalized Gradient Approximation Made Simple. *Phys. Rev. Lett.* **1996**, *77*, 3865−3868.
(46) Monkhorst, H. J.; Pack, J. D. Special Points for Brillouin-Zone Integrations. *Phys. Rev. B* **1976**, *13*, 5188−5192.
(47) Nosé, S. A Molecular Dynamics Method for Simulations in the Canonical Ensemble. *Mol. Phys.* **1984**, *52*, 255−268.
(48) Li, X. X.; Wu, X. J.; Li, Z. Y.; Yang, J. L.; Hou, J. G. Bipolar Magnetic Semiconductors: A New Class of Spintronics Materials. *Nanoscale* **2012**, *4*, 5680−5685.
(49) Pan, H.; Zhang, Y. W.; Shenoy, V. B.; Gao, H. Ab Initio Study on a Novel Photocatalyst: Functionalized Graphitic Carbon Nitride Nanotube. *ACS Catal.* **2011**, *1*, 99−104.
(50) Jose, G.; Peter, K. First Principles Study of $C_3N_4$ Carbon Nitride Nanotubes. *J. Mater. Chem.* **2009**, *19*, 3020−3026.
(51) Chai, G.; Lin, C.; Zhang, M.; Wang, J.; Cheng, W. First-Principles Study of CN Carbon Nitride Nanotubes. *Nanotechnology* **2010**, *21*, 195702.
(52) Miyamoto, Y.; Cohen, M. L.; Louie, S. G. Theoretical Investigation of Graphitic Carbon Nitride and Possible Tubule Forms. *Solid State Commun.* **1997**, *102*, 605−608.
(53) Heyd, J.; Scuseria, G. E.; Ernzerhof, M. Hybrid Functionals Based on a Screened Coulomb Potential. *J. Chem. Phys.* **2006**, *124*, 219906.

(54) Kresse, G.; Furthmuller, J. Efficient Iterative Schemes for ab Initio Total-Energy Calculations Using a Plane-Wave Basis Set. *Phys. Rev. B* **1996**, *54*, 11169−11185.
(55) Kresse, G.; Furthmuller, J. Efficiency of Ab-Initio Total Energy Calculations for Metals and Semiconductors Using a Plane-Wave Basis Set. *Comput. Mater. Sci.* **1996**, *6*, 15−50.
(56) Hu, T.; Hashmi, A.; Hong, J. S. Transparent Half Metallic g-$C_4N_3$ Nanotubes: Potential Multi-Functional Applications for Spintronics and Optical Devices. *Sci. Rep.* **2014**, *4*, 6059.

## ■ NOTE ADDED IN PROOF

After submitting this paper, we became aware of a similar independent work conducted by Hu, Hashmi, and Hong.[56] On the basis of DFT calculation by using the VASP package, they examined the electronic and optical properties of zigzag and armchair g-$C_4N_3$ nanotubes with relatively small diameters. They found that the properties of zigzag SWCNNTs show size dependency and that zigzag $(n, 0)$ tubes with $n = 4$ and 6 show an AFM ground state with band gaps while $(n, 0)$ tubes with $n > 7$ have FM ground states and display half-metallicity. Note that, on the basis of our test calculations at the GGA-PBE level, we find that both ground states of (4, 0) and (6, 0) tubes should be FM. Moreover, they did not investigate the helical SWCNNTs.[56]